AGU PUBLICATIONS

JGR

Journal of Geophysical Research: Planets

RESEARCH ARTICLE
10.1002/2016JE004994

Key Points:
- Time variability of stresses and dynamic disequilibrium affect the initiation of plate tectonics
- Upper thermal boundary layer dynamics are not self-determined; the mantle below matters
- Increasing convective mantle shear stress at the lithospheric base leads into plate failure

Correspondence to:
V. Stamenković,
rinsan@caltech.edu

Citation:
Stamenković, V., T. Höink, and A. Lenardic (2016), The importance of temporal stress variation and dynamic disequilibrium for the initiation of plate tectonics, *J. Geophys. Res. Planets*, *121*, 896–915, doi:10.1002/2016JE004994.

Received 5 JAN 2016
Accepted 29 APR 2016
Accepted article online 11 MAY 2016
Published online 4 JUN 2016
Corrected 20 JUN 2016

This article was corrected on 20 JUN 2016. See the end of the full text for details.

The importance of temporal stress variation and dynamic disequilibrium for the initiation of plate tectonics

V. Stamenković[1,2], T. Höink[3], and A. Lenardic[3]

[1]Department of Geological and Planetary Sciences, California Institute of Technology, Pasadena, California, USA, [2]Jet Propulsion Laboratories, Pasadena, California, USA, [3]Department of Earth Science, William Marsh Rice University, Houston, Texas, USA

Abstract We use 1-D thermal history models and 3-D numerical experiments to study the impact of dynamic thermal disequilibrium and large temporal variations of normal and shear stresses on the initiation of plate tectonics. Previous models that explored plate tectonics initiation from a steady state, single plate mode of convection concluded that normal stresses govern the initiation of plate tectonics, which based on our 1-D model leads to plate yielding being more likely with increasing interior heat and planet mass for a depth-dependent Byerlee yield stress. Using 3-D spherical shell mantle convection models in an episodic regime allows us to explore larger temporal stress variations than can be addressed by considering plate failure from a steady state stagnant lid configuration. The episodic models show that an increase in convective mantle shear stress at the lithospheric base initiates plate failure, which leads with our 1-D model to plate yielding being less likely with increasing interior heat and planet mass. In this out-of-equilibrium and strongly time-dependent stress scenario, the onset of lithospheric overturn events cannot be explained by boundary layer thickening and normal stresses alone. Our results indicate that in order to understand the initiation of plate tectonics, one should consider the temporal variation of stresses and dynamic disequilibrium.

1. Introduction

Plate tectonics is an example of an active lid mode of mantle convection where the lithosphere is mobile and participates in mantle overturn. At the other extreme is a single plate planet, a stagnant lid mode, where the lithosphere does not participate in mantle overturn. At present, plate tectonics is only known to operate on the Earth. In an effort to map the conditions that favor plate tectonics versus a stagnant lid state, various groups have explored mantle convection models that incorporate a viscoplastic rheology [e.g., *Moresi and Solomatov*, 1998; *O'Neill et al.*, 2007; *Tackley*, 2000; *Wong and Solomatov*, 2015]. The rheology allows localized lithosphere failure zones to form. These failure zones serve as analogs for weak plate boundary zones that enable lithosphere overturn. Plate tectonics involves more than the formation of weak plate margins. However, a focus on plate deformation and localized failure allows for conservative mapping of the conditions under which plate tectonics is more or less likely to occur [e.g., *Moresi and Solomatov*, 1998; *Stein et al.*, 2004; *Tackley*, 2000; *Trompert and Hansen*, 1998].

One approach for modeling the initiation of plate tectonics is to start from a stagnant lid model, in steady or statistically steady state, and vary the yield stress until failure occurs [e.g., *Fowler*, 1985; *Foley and Bercovici*, 2014; *O'Neill et al.*, 2007; *Solomatov*, 2004; *Wong and Solomatov*, 2015]. This approach is practical but can minimize the time dependence of mantle stresses. As highlighted by *Wong and Solomatov* [2015], time dependence of stresses might be key in understanding plate tectonics as steady state solutions might break down when a plate approaches yielding.

Our goal is to take a step toward exploring the effects of large temporal stress variations and dynamic disequilibrium. To achieve this, we study the initiation of plate failure with 3-D spherical shell mantle convection models in an episodic mode. An episodic mode can exist in regions of parameter space bounded by temporally continuous plate tectonics and single plate regimes [*Loddoch et al.*, 2006; *Moresi and Solomatov*, 1998; *Turcotte*, 1995]. The episodic mode is characterized by periods of lithosphere stagnation punctuated with global lithospheric overturn events. The episodic mode allows for large stress variations about a mean value

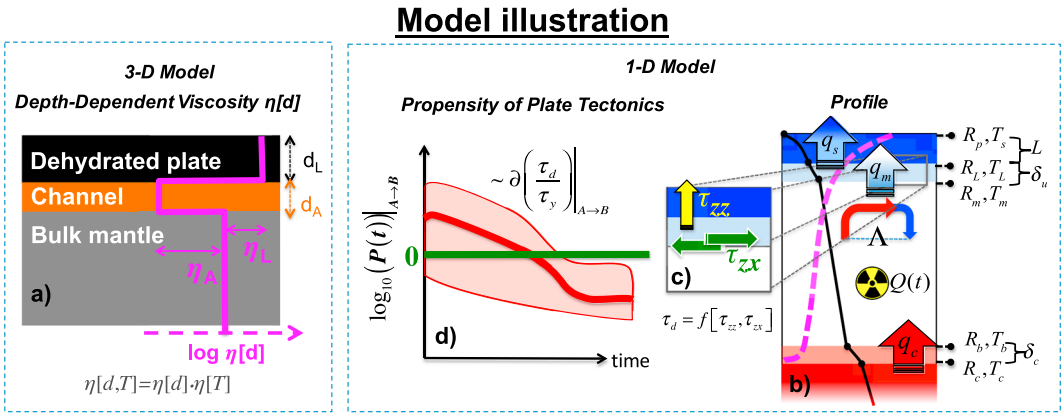

Figure 1. Illustration of 3-D and 1-D models: (a) 3-D depth-dependent part of the mantle viscosity: we include below a dehydrated chemical lithosphere a low-viscosity channel above a lower bulk mantle. We vary the ratios of the channel to lower mantle viscosity within $\eta_A = 1/30-1/100$ and the channel thickness to mantle depth within $d_A = 0.122-0.455$. The relative viscosity of the dehydrated chemical lithosphere to the reference lower mantle value was $\eta_L = 10$ and the relative thickness of the dehydrated chemical lithosphere to mantle depth was $d_L = 0.1$. 1-D model: (b) A stagnant lid of thickness L is above an upper thermal boundary layer of thickness δ_u. The temperature is adiabatic between the base of δ_u and R_b due to vigorous convection (an isotherm, mimicking our 3-D model Boussinesq approximation, does not affect our 1-D results). The mantle is heated by decaying radiogenic heat sources $Q[t]$ and from the core by q_c. The convective heat flux out of the mantle q_m is transported conductively through L leading to the surface heat flux q_s. The depth profile of temperature (solid black) and viscosity (dashed purple) for temperature-dependent viscosity are shown. Λ is the length of convective cells (approximately plate length). (c) The driving stress for plate yielding τ_d is composed of normal τ_{zz} and shear stress τ_{zx} versus the depth-dependent Byerlee yield stress τ_y. (d) Illustration of the decimal logarithm of the propensity of initiating plate tectonics for a change of a planet condition from A → B. The sum of $\log_{10}P(t)$ curves for all planets forms a "propensity of initiating plate tectonics versus time phase space" (shaded red), in which we highlight one individual $\log_{10}P(t)$ curve (in solid red). Positive (negative) values of $\log_{10}P(t)$ indicate that the change increased (decreased) the effectiveness of initiating plate yielding (τ_d/τ_y). For parameter values see Tables 1–3.

(in time and in space). We also use 1-D thermal history and plate yielding models to explore how the results from our 3-D experiments affect inferences regarding the comparative tectonic evolution of terrestrial planets.

2. Methods

In the following, we provide an overview of our methods (see Figure 1 for illustration). For fuller descriptions, the interested reader is directed toward *Höink et al.* [2012] for the 3-D models and for the 1-D models to *Stamenković and Breuer* [2014] and *Stamenković et al.* [2012]. All scalings needed to reproduce our 1-D results can be found in the appendix. Our 3-D model results are based for practical reasons on nondimensional values, with standard nondimensionalization factors used in mantle convection simulations [e.g., *Christensen*, 1984], whereas our 1-D model is based on dimensional values.

In our 3-D modeling, we included a dehydrated lithosphere above a weak upper mantle channel (see Figure 1a). We did not include such additional viscosity layers in our 1-D model in order to minimize its complexity and to be able to relate to previous thermal history and plate tectonics models, which did not include any channeling effects. We discuss later the implications of channels.

2.1. Time-Dependent 3-D Spherical Shell Convection Model

We performed numerical convection experiments, assuming the Boussinesq approximation, in 3-D spherical shell geometry. The standard hydrodynamic partial differential equations of mantle flow are solved using the spherical code CitcomS [*Tan et al.*, 2006; *Zhong et al.*, 2000] with free-slip boundary conditions at top and bottom surfaces.

We focus on the five numerical experiments from *Höink et al.* [2012] that displayed episodic behavior. Those experiments were used to track the evolution of shear τ_{zx} and normal τ_{zz} stresses through tectonic mode transitions. All parameters needed to reproduce the 3-D calculations are provided in Table 1. In Table 2 all 3-D numerical runs are specified—this includes the five runs in the episodic regime as well as one run in a plate tectonics like mode of convection and one in a stagnant lid regime. The episodic mode is a useful test bed to study the time evolution of stresses and to track multiple events to ensure that results are consistent over long times and are not overly sensitive to model initialization.

Table 1. Three-Dimensional Model Parameters Used in This Study to Describe Mantle Convection for a Planet With a Low-Viscosity Asthenosphere, a Dehydrated High-Viscosity Lithosphere, and a Bulk Lower Mantle Viscosity With Nondimensional Reference Viscosity η_0 Assuming Temperature-Dependent Viscosity With a 4 Orders of Magnitude Variation From the Top to the Bottom Temperature (See Figure 1a)

Parameter	Description	Value	Units
R_p	Planet radius	6371	km
R_c	Core radius	3504	km
D	Mantle depth	2867	km
g	Gravity	10	$m\ s^{-2}$
ρ	Mantle rock density	3500	$kg\ m^{-3}$
κ	Mantle thermal diffusivity	10^{-6}	$m^2\ s^{-1}$
α	Mantle thermal expansivity	3×10^{-5}	K^{-1}
C	Mantle heat capacity (at constant pressure)	1250	$Jkg^{-1}\ K^{-1}$
Ra	Rayleigh number with standard definition for basally heated systems using the viscosity at the mantle base	10^5	–
H	Nondimensional internal heating rate	60	–
$Q_{3\text{-}D}$	Associated dimensional heating rate	3.6×10^{-14}	$W\ kg^{-1}$
$\Delta\eta_T$	Temperature related viscosity contrast	10^4	–
d_A	Low-viscosity zone thickness to mantle depth ratio	0.122–0.455	–
d_L	Dehydrated chemical lithosphere thickness to mantle depth ratio	0.1	–
η_A	Nondimensional reference viscosity ratio between asthenosphere and lower mantle	1/30–1/100	–
η_L	Nondimensional reference viscosity ratio between dehydrated chemical lithosphere and lower mantle	10	–
η_0	Nondimensional reference viscosity of lower mantle	1	–
η_{ref}	Dimensional reference viscosity of lower mantle	10^{21}	Pa s
$\tau_{y,3\text{-}D}$	Nondimensional yield stress	1.36×10^4	–
$\tau_{y,3\text{-}D,dim}$	Associated dimensional yield stress	16.55	MPa
ΔT	Associated dimensional temperature contrast over mantle	4	K
nz	Number of vertical finite-element nodes	33–65	–

The experiments incorporate a temperature- and depth-dependent Arrhenius-type viscoplastic rheology in a model of thermally driven convection for a mix of basal and internal heating. The temperature- and depth-dependent nondimensional viscosity $\eta[T, d]$ is:

$$\eta = \left(\eta[d, T]^{-1} + \eta_y^{-1}\right)^{-1} \tag{1}$$

$$\eta_y = \tau_{y,3\text{-}D}(2\dot{\epsilon})^{-1} \tag{2}$$

Table 2. Summary of 3-D Runs: η_A Is the Viscosity of the Channel in Relation to the Lower Mantle Viscosity; d_A Is the Thickness of the Channel in Relation to the Whole Mantle Depth; the Nondimensional Internal Heating Rate Is $H = 60$ and the Rayleigh Number (Standard Definition for Basally Heated Systems Using the Viscosity at the System Base) Is 10^5; the Period Is Defined as the Average Time (in Units of Overturn Time) Between Overturn Events; σ Is the Standard Deviation of the Period; and the Overturn Time Is Defined as the Inverse of the Whole Mantle (Depth 0–0.45) Averaged Nondimensional RMS Velocity—This Corresponds to How Much Time a Parcel Needs on Average to Travel Across the Mantle (Computed Over the Entire Time After Statistically Steady Has Been Reached in Mobile and Stagnant Cases, and Over Several Resurfacing Events and Quiescence Periods in Episodic Cases). The channel number is defined as $MN = \eta_A/(d_A)^3$ and seems to be an indicator of the tectonic mode (see section 4.1 and Figure 8)

Run ID	η	d	Period	σ	Nondimensional Overturn Time	No. of Vertical Nodes	See Regime	Channel Figure Nos.	Number MN
1. FBRun5lA30-96	1/30	0.122	1.0	0.0	0.002057	65	Mobile	3a, 5a, 8	18.4
2. FBRun5lA30D015-12	1/30	0.233	2.625	0.303	0.001661	33	Episodic	3b, 5b, 8	2.6
3. FBRun5lA30D015-96	1/30	0.233	2.5	1	0.00158	65	Episodic	4	2.6
4. FBRun5lA30D020-12	1/30	0.344	4.812	0.583	0.000761	33	Episodic	5c, 8	0.8
5. FBRun5lA30D020-48	1/30	0.344	1.13	0.1	0.003499	65	Episodic	6	0.8
6. FBRun5lA100D015-12	1/100	0.233	18.9	1.4	0.001971	33	Episodic	3d, 5d, 8	0.8
7. FBRun5lA30D025-12	1/30	0.455	8	0.0	0.003668	33	Stagnant	3c, 5e, 8	0.4

η_y is the nondimensional viscosity where yielding occurs, $\tau_{y,3\text{-D}}$ is the prescribed nondimensional yield stress for our numerical 3-D experiments, and $\dot{\epsilon}$ is the second invariant of the strain rate tensor. The nondimensional activation energy E' was set to allow for a 4 orders of magnitude variation of the nondimensional temperature-dependent part of the viscosity $\eta[T]$ from the top to the bottom temperature, where T is the nondimensional temperature, which varies from 0 to 1 from the top to the bottom of the mantle.

$$\eta[d,T] = \eta[d]\eta[T] = \eta[d]\exp[E'(T+1)^{-1} - E'/2] \tag{3}$$

The depth dependence of the nondimensional viscosity $\eta[d]$ allowed for a low-viscosity channel in the upper mantle ($\eta[d] = \eta_A$) between an intermediate viscosity lower mantle ($\eta[d] = \eta_0 = 1$) and an uppermost high-viscosity dehydrated chemical lithosphere ($\eta[d] = \eta_L$) (see Figure 1a). The high-viscosity dehydrated layer is associated with melt extraction and dehydration [*Hirth and Kohlstedt*, 1996].

The mantle depth is in nondimensional values 0.45, and the nondimensional value for the planet radius is 1. The ratio of the upper channel to lower mantle viscosity was varied within $\eta_A = [1/30, 1/100]$, and the thickness of the channel was changed within $d_A = [0.122, 0.455]$ in relation to the mantle depth. The dehydrated chemical lithosphere viscosity η_L was 10 times the reference lower mantle value, and its nondimensional thickness in relation to the mantle depth was $d_L = 0.1$.

The Rayleigh number (standard definition for basally heated systems using the viscosity at the system base) and the nondimensional internal heating rate in our 3-D model are

$$Ra_{3\text{-D}} = \alpha\rho g D^3(\Delta T)(\kappa\eta_{\text{ref}})^{-1} \tag{4}$$

$$H = Q_{3\text{-D}}D^2(\kappa C\Delta T)^{-1} \tag{5}$$

With 3-D parameter values in dimensional form specified in Table 1, such as the mantle thermal expansivity α, the mantle density ρ, the mantle depth from top to bottom D, the mantle temperature contrast ΔT, the reference viscosity at the mantle base η_{ref}, the thermal diffusivity κ, the rate of radiogenic heat generated per unit mass $Q_{3\text{-D}}$, and the mantle specific heat capacity at constant pressure C. The nondimensional and dimensional values for our 3-D parameters are summarized in Table 1.

We fixed the basal temperature to a constant value (nondimensional = 1), the nondimensional internal heating rate to $H = 60$, and the Rayleigh number to 10^5. The choice of model parameters is similar to the ones of *Foley and Becker* [2009].

Our goal is to explore numerical experiments that can give insights into stress evolution within a convecting system, as opposed to simulating the Earth (which, for reasons of numerical resolution and available computer power, we cannot do at this stage). We can dimensionalize model values with equations (4), (5), and using $\sigma_{y,3\text{-D,dim}} = \sigma_{y,3\text{-D}}\eta_L\kappa D^{-2}$ [e.g., *O'Neill and Lenardic*, 2007] (see Table 1). However, the dimensional values should not be overinterpreted, as the numerical experiments are run at levels of convective vigor lower by roughly 2 orders of magnitude relative to estimates for present day Earth. Indeed, this restriction is one of the reasons we need, at this stage, to combine insights from numerical experiments with our 1-D modeling approach, which can be used to explore arbitrarily high degrees of convective vigor and, as such, can be run assuming dimensional values appropriate for present day Earth, deep time Earth, and for planets with much higher degrees of convective vigor than the Earth.

We have added a specific metric tracking analysis to the experiments of *Höink et al.* [2012] that showed episodic behavior. Changes between stagnant and active lithosphere states were tracked using velocity profiles, the nondimensional surface heat flux (Nusselt number), the upper thermal boundary layer thickness (corresponding to the point at which the geotherm transitions to the internal well mixed gradient—so the purely conductive lid plus the thermal sublayer), average internal temperature, the mobility, and the velocity ratio. Mobility Mob is defined as the horizontal RMS surface velocity u^0_{rms} divided by the average RMS velocity at LAB $v^{\text{LAB}}_{\text{rms}}$:

$$\text{Mob} = \frac{u^0_{\text{rms}}}{v^{\text{LAB}}_{\text{rms}}} \tag{6}$$

The lithosphere-asthenosphere boundary (LAB) is defined as the vertical location of the azimuthally averaged profiles where the viscosity gradient is maximal. Stresses were calculated at each time step. The velocity ratio VR is defined as the peak parabolic component Γ of the velocity profile within the low-viscosity channel over the RMS velocity at the surface u^0_{rms}:

$$\mathrm{VR} = \frac{\Gamma}{u^0_{\mathrm{rms}}} \tag{7}$$

For plotting purposes, we use the nondimensional overturn time, which is defined as the inverse of the whole mantle averaged nondimensional RMS velocity.

Shear τ_{xz} and normal τ_{zz} stresses were computed using radial profiles of horizontally averaged viscosity at the LAB (no vertical averaging was performed), the radial gradient of azimuthal velocity, and the radial gradient of vertical velocity.

2.2. One-Dimensional Model in a Nutshell

We compute the interior thermal profiles, viscosities, convective velocities, and stresses driving plate failure τ_d or resisting plate yielding τ_y of rocky planets during 13 Gyr (approximtely the age of the universe) with an extended 1-D boundary layer model, which is coupled to energy conservation in the mantle and core and to a conductive growth equation for the stagnant lid based on *Stamenković et al.* [2012] [similar to *Grott and Breuer*, 2008]. All variables, parameter values, and scaling laws needed to reproduce our 1-D results are provided in Appendix A.

We determine the effectiveness of initiating plate yielding as a function of time, which we call the propensity of initiating plate tectonics $P[t]$ for a change from a planet condition "A" to "B," such as for an increase in planet mass or radiogenic heat concentration.

$$\begin{aligned} X &= \tau_d/\tau_y \\ P(A \rightarrow B) &= X(B)/X(A) \end{aligned} \tag{8}$$

The propensity of initiating plate tectonics is defined via a failure function X, which is the ratio of the driving stress τ_d created by mantle convection (generally a mixture of shear and normal stresses) versus the depth-dependent Byerlee-type yield stress τ_y holding the plate together. By plotting the decimal logarithm of the propensity of initiating plate tectonics, we can illustrate how a change in a planet condition from A to B affects the potential of plate yielding: as an example, by computing the propensity of initiating plate tectonics for an increase in planet mass from an one Earth mass to a 10 Earth mass planet, we compute how the ratio of driving stress versus yield stress is affected by planet mass. Positive values of $\log_{10}P$ indicate that the change in planet condition (e.g., larger planet mass) has increased the potential for plate yielding, negative values indicate that the change has suppressed plate yielding (see Figure 1d for illustration).

We allow for a wide range of model parameters that approximate various rocky planet mantle compositions (dry, wet, a radiogenic heat source concentration per unit mass 0.1–10 times the Earth reference value), varied Fe, Mg content in mantle rock), structures (from coreless to Mercury structure), surface temperatures (from 288 K to 1000 K), planet masses (1–10 Earth masses), and initial conditions [from a mantle starting with an adiabatic interior temperature profile ("cool") to the mantle solidus ("hot"), for exact initial temperature values see Table 3 in *Stamenković et al.*, 2012]. Melting temperatures for mantle rock come from the theoretical predictions of *Stamenković et al.* [2011], which are in good agreement with experimental data from *McWilliams et al.* [2012]. The motivation for a wide parameter space study lies in the goal to determine which conclusions are robust for a large family of rocky planets.

This wide parameter space sweep lead us to compare ~20,000 different models in order to study how plate yielding (or the propensity of initiating plate tectonics) depends on radiogenic heat content and planet mass. Table 3 shows the varied parameter space values and Earth reference values for our 1-D model.

For illustration purposes, we combine the propensity of initiating plate tectonics evolution curves for all cases that explore how a variation in a planet condition affects plate yielding. All those curves form a "propensity envelope" from which individual evolution curves can be highlighted, as illustrated in Figure 1d.

Table 3. One-Dimensional Parameter Space (Relative Values Are Referenced to Average Earth Values): (1): *Turcotte and Schubert* [2002]; (2): *Stevenson et al.* [1983]; (3): *Stamenković et al.*[2011]; (4): *Buffett et al.* [1996]; (5): *Escartin et al.* [2001]; (6) *Stamenković and Seager* [2016]

1-D Model Parameters

Variable	Physical Meaning	Value	Units	Reference
	Standard Earth Parameters			
$M_\oplus$	Earth mass	$5.974 \cdot 10^{24}$	kg	1
$T_{S,\oplus}$	Mean Earth surface temperature	288	K	–
$R_{p,\oplus}$	Mean Earth planetary radius	6371	km	1
$R_{c,\oplus}$	Mean Earth core radius	3480	km	1
$f_{c,\oplus}$	Earth core mass fraction	0.3259	–	1
$k_{m,\oplus}$	Average Earth mantle thermal conductivity	4	$Wm^{-1}\,K^{-1}$	2
$\alpha_{m,\oplus}$	Average Earth mantle thermal expansivity	2×10^{-5}	K^{-1}	2
$E^*_\oplus$	Earth mantle rock activation energy	300	$kJ\,mol^{-1}$	3
T_{ref}	Reference temperature for viscosity	1600	K	3
$\tilde{\eta}_{\text{ref},\oplus}$	Earth mantle reference viscosity	10^{21}	Pa s	3
Ra_{crit}	Critical Rayleigh number	1000	–	1
$\rho_{\text{up},\oplus}$	Average Earth lithosphere density	3500	$kg\,m^{-3}$	1
$C_{m,\oplus}$	Average Earth mantle heat capacity (at const. pressure)	1250	$Jkg^{-1}\,K^{-1}$	3
$C_{c,\oplus}$	Average Earth core heat capacity (at const. pressure)	800	$Jkg^{-1}\,K^{-1}$	4
$C_{\text{fric},\oplus}$	Average Earth-like lithospheric friction coefficient	0.15	–	5
	Variation in Planet Mass, Composition, Structure, and Surface Temperature			
M	Relative planet mass	1—10	$M_\oplus$	6
T_S	Surface temperature	288–1000	K	6
f_c	Core mass fraction	0–0.65	–	6
k_m	Relative mantle thermal conductivity	0.5–2	$k_{m,\oplus}$	6
α_m	Relative mantle thermal expansivity	0.5–2	$\alpha_{m,\oplus}$	6
C_m	Relative mantle heat capacity (at const. pressure)	0.5–2	$C_{m,\oplus}$	6
E^*	Relative mantle activation energy	0.6–1.4	$E^*_\oplus$	6
$\tilde{\eta}_{ref}$	Relative mantle reference viscosity	10^{-5}–10^5	$\tilde{\eta}_{\text{ref},\oplus}$	6
C_{fric}	Relative lithospheric friction coefficient	0.1–10	$C_{\text{fric},\oplus}$	6
Q	Relative radiogenic heat source concentration per unit mass	0.1–10	$Q_\oplus$	6

3. Results

In section 3.1, we show our results based on a steady state approach, and in section 3.2 we show how these results change based on the episodic mode approach.

3.1. Stagnant Lid Mode, Steady State, and a Normal Stress World

In section 3.1.1, we review the nature of stresses governing plate failure for the standard steady state stagnant lid approach for the initiation of plate tectonics and show in section 3.1.2 with our 1-D model the implications of this classic approach for plate yielding as a function of radiogenic heat content and planet mass.

3.1.1. A Normal Stress World

Modeling the initiation of plate tectonics can be approached by assuming steady state stagnant lid convection and varying the yield stress until failure is reached. Failure is reached if the driving stress caused by mantle convection τ_d reaches a characteristic plate yield stress τ_y [e.g., *Moresi and Solomatov*, 1998]. Often, a *von Mises* [1913] formulation is followed such that the value of the second invariant of the deviatoric stress tensor determines when failure occurs. To illustrate this process, we can imagine a two-dimensional convective system with horizontal x axis and vertical z axis in steady state. The driving stress τ_d scales with deviatoric normal τ_{xx} and deviatoric shear stress τ_{zx} in horizontal direction. With local mass conservation and balance of moments of inertia, we obtain $\|\tau_{xx}\| = \|\tau_{zz}\|, \|\tau_{zx}\| = \|\tau_{xz}\|$.

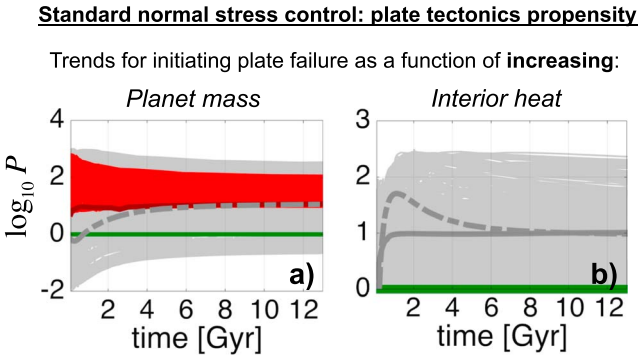

Figure 2. Impact of (a) increasing planet mass and (b) increasing radiogenic heat content on the propensity of initiating plate tectonics for the standard normal stress model during 13 Gyr for planets with variable planet structure, composition, and initial conditions. Negative (positive) values represent the initiation of plate tectonics being suppressed (supported) by increasing planet mass (or radiogenic heat content) (green line indicates neutral zero). In Figure 2a planet mass is increased from 1 → 10 Earth masses ($M = 1 \rightarrow M = 10$). Coloring represents different initial temperature assumptions: (gray) the initial temperature profile of the $M = 1, 10$ planets is anywhere between an adiabat and the mantle solidus, (red) initial interior temperature for $M = 1, 10$ is along the mantle solidus. Above this phase space, we plot two individual propensity evolution curves: (dark red) for our Earth model increasing planet mass to $M = 10$ with both planets starting along mantle solidus; (dashed gray) like the dark red line but $M = 10$ starts along adiabat. In Figure 2b the initial radiogenic heat concentration Q per unit mass is increased for values of 0.1, 0.2, 0.5, 1, 5 to 10 times the initial Earth reference concentration; results plotted for $M = 10$ planets (same result for $M = 1$). Solid (dashed) dark gray line represents an increase of $Q = 1 \rightarrow 10$ for our Earth model starting along the mantle solidus (for $M = 10$, Earth-like in structure and composition starting along the adiabat).

Based on modeling plate tectonics initiation from a steady state stagnant lid scenario, stresses can be approximated as weakly time dependent and the theory of *Fowler* [1985] is applicable: a force balance between basal shear τ_{zx} and normal lid stresses τ_{xx} in the horizontal direction allows the normal lid stress to be computed as a function of basal shear stress.

$$\|\tau_{zz}\| = \|\tau_{xx}\| = \|\tau_{zx}\|\Lambda L_T^{-1} \qquad (9)$$

Λ is the length of convective cells (approximately plate length) and L_T is lithosphere thickness. Based on this force balance, normal stresses are greater than basal shear stresses, as the horizontal scale of convective cells Λ is much larger than the lithospheric thickness [see, e.g., *Solomatov*, 2004]. The large lithospheric viscosity gradients due to the temperature dependence of the viscosity additionally increase the ratio of peak normal versus basal shear stress in the lithosphere (see *Solomatov* [2004] and our section 4.3).

Therefore, for the steady state approach, the driving stress causing failure can be approximated by normal stresses in the plate $\tau_d = \tau_{zz}$ [e.g., *Fowler*, 1985; *Foley and Bercovici*, 2014; *Solomatov*, 2004; *Turcotte*, 1995; *Wong and Solomatov*, 2015].

3.1.2. Implications of a Normal Stress World

We can now use our 1-D model to explore how the propensity of initiating plate tectonics depends on increasing planet mass and increasing radiogenic heat content under the assumption that normal stresses dominate plate failure, $\tau_d = \tau_{zz}$. The results depend on the values for the Nusselt-Rayleigh scaling parameter for the mantle heat flux q_m (β, where $q_m \sim Ra^{\beta}$), the scaling parameter for the convective velocity v_c (γ, where $v_c \sim Ra^{\gamma}$), and the scaling parameter for the convective cell length Λ (~plate length) (ϵ, where $\Lambda \sim \mathrm{Ra}^{-\epsilon}$), with Ra the 1-D model Rayleigh number defined in Appendix A.

In the following, we focus on a model with a constant Λ (hence, $\epsilon = 0$), which is often assumed [e.g., *Foley and Bercovici*, 2014; *Foley et al.*, 2012; *O'Neill et al.*, 2007; *O'Rourke and Korenaga*, 2012; *Solomatov*, 2004; *Valencia et al.*, 2007]. To illustrate our results, we choose the parameters $\beta = 1/3$ and $\gamma = 2/3$ for the scaling of the heat flux and convective velocity with Rayleigh number (equations (A2) and (A5)). Other reasonable values of β and γ do not change the conclusions presented below [see *Stamenković and Breuer*, 2014, Figures 3 and 8]. We name this model the "standard normal stress model."

We illustrate our results for the standard normal stress model in Figure 2. Figure 2a plots, for all cases considered, the propensity of initiating plate tectonics curves as a function of time for an increase of planet mass from 1 to 10 Earth masses. All evolution curves are combined to form a "propensity envelope" phase space. Gray zones in Figure 2 correspond to planets where we made no assumptions on initial thermal conditions (planets can start with interior temperatures anywhere between the mantle solidus and adiabatic interior temperatures). The red zone represents the scenario where all planets start along the solidus. Figure 2b plots propensity curves for increasing initial radiogenic heat concentrations (values of 0.1, 0.2, 0.5, 1, 5 to 10 times the initial Earth reference concentration $Q[t]$ in W/kg have been compared). Negative (positive) values of $\log_{10} P(t)$ indicate that an increase of planet mass or interior heat is hindering (supporting) the initiation of plate tectonics based on our failure criterion.

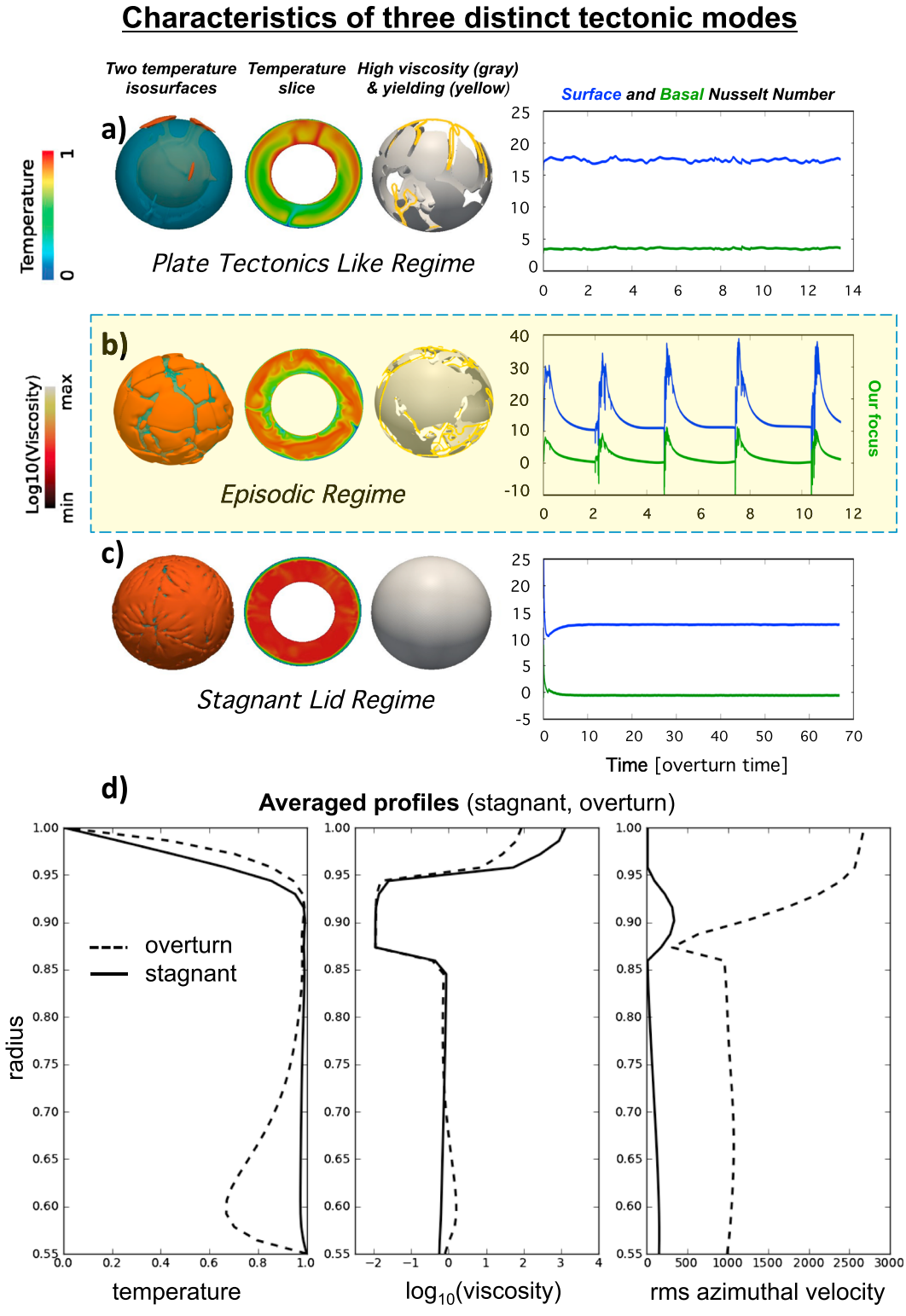

Figure 3. Results from our 3-D spherical numerical experiments that settled into three convection regimes: (a) active surface layer that maintains piecewise constant horizontal surface velocity (Run 1, see Table 2); (b) episodic mode with periods of active lithosphere overturn and periods of lithosphere quiescence-planet cross sections show an overturn event (Run 2); (c) a regime in which the lithosphere did not participate in convective overturn (Run 7). Nusselt number (~nondimensional heat flux) values as a function of time (in units of overturn time) are shown. (d) We compare for different states before and during an overturn event for an episodic case (Run 6) the azimuthally averaged profiles of temperature, viscosity, and azimuthal velocity; nondimensional mantle depth is 0.45.

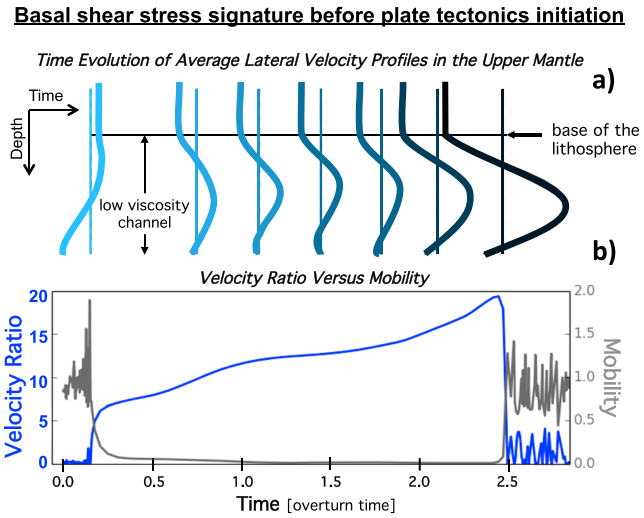

Figure 4. Basal shear stress builds up leading into an overturn event: Tectonic mode transitions, metrics, and velocity profiles from a 3-D spherical numerical experiment that settled into an episodic mode of mantle convection. (a) time series velocity profiles with depth from the surface to the base of the asthenosphere. (b) The vertical line associated with each velocity profile (of same color) extended downward to the nondimensional time axis indicates the associated time step; b) surface mobility, and velocity ratio. Time is shown in overturn times. Run 3 used here is basically same as Run 2 from Figure 3b with a higher spatial resolution. As shown in Table 2, there is almost no difference in results for the higher resolution case.

For the normal stress model, the initiation of plate tectonics is more likely with increasing interior heat, as all propensity of plate tectonics values are positive independent of planet mass, composition, structure, or initial conditions (Figure 2b). Also, the initiation of plate tectonics is more likely for more massive planets if all planets start along the solidus, as the red zone in Figure 2a, which is the sum of all propensity of initiating plate tectonics evolution curves when planets start along or above the solidus, is also always positive. This is also valid if all planets start along an adiabat. If planets can form anywhere between cool adiabatic and hot solidus initial temperatures, then it is not clear whether an increase in planet mass supports or suppresses the initiation of plate tectonics, as the gray zone in Figure 2a, which corresponds to no assumptions on initial temperatures, is not uniquely positive or negative.

The standard normal stress model predicts plate failure to be more likely with increasing interior heat and for more massive planets because in this case the propensity for plate failure scales principally with convective velocities (assuming a constant depth scale $\tilde{D}$, see equations (A5) and (A6)), which increase with interior temperatures. As more massive planets are generally hotter, this implies they are more likely to initiate plate tectonics (assuming that initial conditions scale similarly with planet mass, so that all planets start either along the solidus or along the adiabat). These results are in agreement with 1-D models that studied plate tectonics on super Earths and assumed normal stresses as the driving stresses for plate failure [*Foley et al.*, 2012; *Foley and Bercovici*, 2014; *Korenaga*, 2010; *O'Rourke and Korenaga*, 2012; *Valencia et al.*, 2007].

3.2. Episodic Mode, Time-Dependent Stresses, and the Rise of Basal Shear Stress

In section 3.2.1, we use our numerical experiments in the episodic mode to explore which stresses initiate an active lid mode under thermal disequilibrium conditions with large temporal stress variations. In section 3.2.2, we then reanalyze our previous 1-D model results (section 3.1.2) based on our new 3-D findings.

3.2.1. Increasing Basal Shear Stress Leads Into Plate Failure

Figure 3 shows three cases from our numerical experiments: plate tectonics like, episodic, and stagnant lid regimes. Episodic behavior is characterized by recurring global lithosphere overturn events and periods of quiescence. Figure 3d plots geotherms for an episodic case at different times.

Figure 4 shows how mobility changes from near zero before an overturn event to a fluctuating value centered around unity during the active lithosphere phase (Figure 4b). The velocity ratio is also fluctuating near unity during the active phase (Figure 4b, far right) and increases during the stagnant lithosphere phase, indicating that the mantle flow velocities below the lithosphere exceed surface velocities.

Five overturn events are shown in the time histories of surface heat flux (Nusselt number) in Figures 3, 5, and 6—the latter also shows time histories of internal temperature, normal, and shear stress at the base of the plate, thermal boundary layer thickness, and the velocity ratio. Each overturn event is associated with increased surface heat flow, decreasing internal temperature, and decreasing upper thermal boundary layer thickness; periods of quiescence are associated with decreasing surface heat flow, increasing internal temperature, and increasing thermal boundary layer thickness (Figure 6). As shown in the Appendix of *Höink et al.* [2012], we found no significant differences between experiments with 33 and 65 vertical nodes.

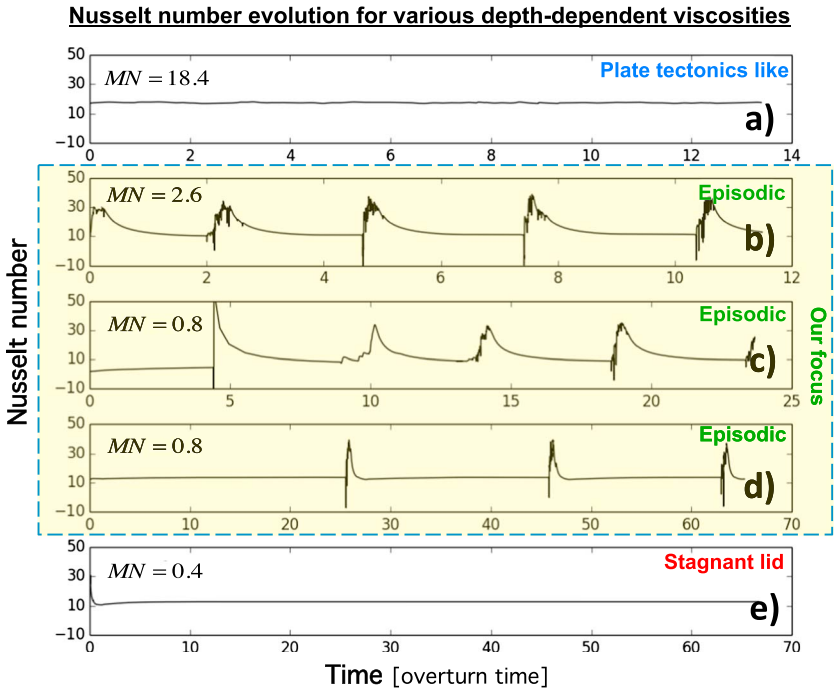

Figure 5. Time series for five runs: Nusselt number time evolution for three 3-D spherical numerical experiment that settled into an episodic mode of convection and two that settled in a plate tectonics like and stagnant lid mode of convection, respectively. From top to bottom (plate tectonics like to stagnant lid), (a) Run 1 (plate tectonics like), (b) Run 2 (episodic), (c) Run 4 (episodic), (d) Run 6 (episodic), and (e) Run 7 (stagnant lid). The approximate channel number is also plotted defined as MN = η_A/d_A^3. We focus on numerical experiments in the episodic regime, compare with Figures 6 and 8. Time is shown in overturn times.

Characteristic periods varied only by a few percent (as an example, see Table 2 for Runs 2 and 3) indicating that the experiments were not underresolved numerically for the parameter conditions explored.

Velocity profiles show a plate driven flow signature during overturn events (see Figure 4a). The active lithosphere drives shear flow in the lower viscosity upper mantle below the plate. During the stagnant phase, the velocity profiles show the signature of a pressure driven flow in the lower viscosity upper mantle [*Höink et al.*, 2011].

After an overturn event, the upper boundary layer progressively thickens (Figure 6). As it thickens into the low-viscosity upper mantle, pressure gradients are generated due to lateral temperature and associated density variations. The dynamics of this pressure driven flow, along with theoretical scalings calibrated against numerical experiments, are discussed in *Höink et al.* [2011]. The velocity profiles document increasing basal shear stress, on the high-viscosity lithosphere, as the magnitude of pressure driven flow increases (Figure 4a). Once lithospheric failure occurs, and an overturn event is initiated, velocity profiles switch to a plate driven flow signature.

As indicated by the surface heat flow, an overturn event is not instantaneous but occurs over a finite period of time, which is smaller than the period of quiescence that separates recurrent overturns (Figures 5 and 6). At the onset of an overturn event, the immobile surface experiences localized fluctuations of stress and strain that can exceed the global average value. This ultimately leads to localized failure as the background average stress values, and by association localized peak values, grow (Figure 3). Once failure zones form, parts of the cold plate can subduct and drag along adjacent plate material while warmer material replaces the subducted plate. Stresses transmitted from this motion, as well as the internal reorganization of temperature differences, causes further destabilization of other parts of the surface. This process continues at different parts of the mantle, until the interior has been cooled to the extent that the vigor of thermal convection is temporarily reduced. Figure 3b shows a snapshot of one hemisphere during an overturn event in the episodic mode, depicting clearly different patches of high viscosity (plates), which do not accommodate strain. Instead, strain

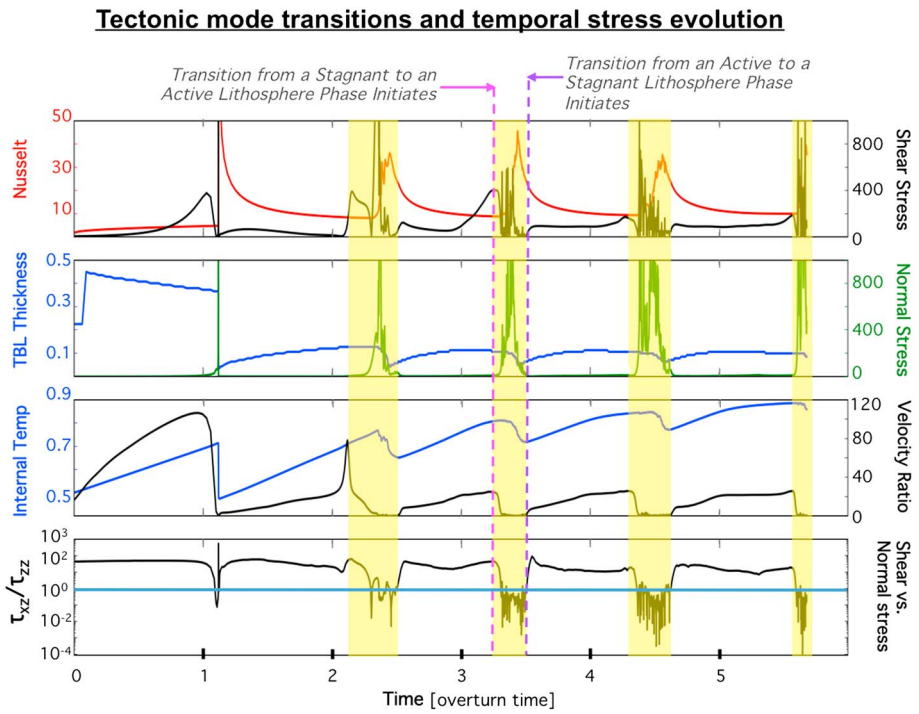

Figure 6. Lead of basal shear stress driving the transition from stagnant to active lid for a system far from thermal equilibrium: Time series diagnostics for transitions between periods of stagnant lid and plate tectonics like behavior from a 3-D spherical numerical experiment that settled into an episodic mode of convection. We show, in nondimensional form, the evolution of Nusselt number, thermal boundary layer thickness (in relation to mantle depth), internal temperature, shear and normal stress computed at the LAB, the velocity ratio, and the decimal logarithm of the ratio of shear stress versus normal stress at the LAB (in the latter, a light blue line indicates where normal stress and shear stress are equal). Transitions from a stagnant to an active mode occur when the velocity ratio drops from large values to ~1 (dashed pink line, compare with Figure 4b). This transition is causally driven by an increase in basal shear stress, normal stresses increase later. Values are shown in dimensionless form; time is in overturn times. Run 5 is used; its channel number is 0.8 (see Table 2).

is accommodated in those regions that currently experience subduction and replacement by warmer material of lower viscosity, which leads to localized minima and maxima of surface heat flux.

At the end of an overturn event, the thermal boundary layer begins to thicken anew and surface heat flow decreases. Both our simulations and previous work show a similar trend in surface heat flux. As discussed by *Lenardic and Kaula* [1994], the vigor of convection declines during this period as the cold lithosphere that has just arrived in the lower mantle leads to a stable density stratification that weakens as the subducted lithosphere is heated. At the same time, a new conductive lithosphere is growing at the surface.

In an episodic mode, each overturn event resets the thermal boundary layer thickness, after which it increases again with time (Figure 6). The progressive growth of the thermal boundary layer leading up to an overturn event has been thought to provide the opportunity for the development and growth of local boundary layer instabilities, which in turn can destabilize the thermal boundary layer and cause its large-scale overturn [*Turcotte*, 1995]. That hypothesis, for the initiation of episodic overturn, is based on classic boundary layer stability analysis [*Fowler*, 1985; *Howard*, 1966]. The boundary layer is assumed to thicken until the growing negative buoyancy of the boundary layer outweighs its rheological resistance to flow. At that critical point, the boundary layer is assumed to become unstable, and assuming boundary layer dynamics are totally self determined, a local boundary layer stability analysis can be used to determine when instability initiates.

If indeed fully self determined local boundary layer stability analysis is applicable, then mantle generated shear stresses below the boundary layer itself do not play a significant role. Our results are not consistent with that idea. The thermal boundary layer reached a maximal thickness independent of internal mantle temperature well before instability initiated (Figure 6). This indicates that boundary layer thickening is not the sole

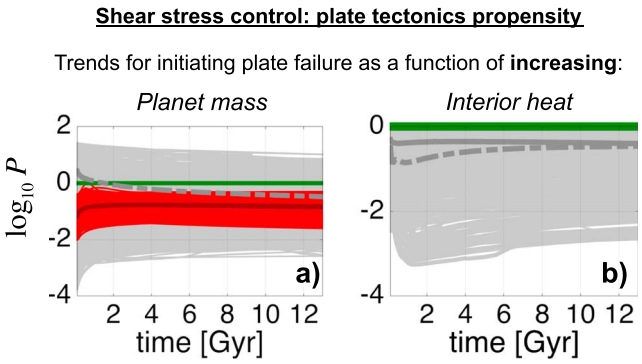

Figure 7. Impact of (a) increasing planet mass and (b) radiogenic heat content on the propensity of initiating plate tectonics for the basal shear stress model during 13 Gyr for planets with variable planet structure, composition, and initial conditions. Behavior is contrary to the standard normal stress model shown in Figure 2. Here increasing planet mass and interior heat generally suppress the initiation of plate tectonics. Nomenclature is identical to Figure 2.

trigger for the initiation of plate failure. The numerical experiments showed a progressive buildup of convective shear stress underneath the immobile plate leading into a failure event (Figures 4 and 6). The failure started initially in localized regions and then propagated in response to convective downflow altering the stress state of the system (Figure 3b).

A crucial point is to compare our results with an often invoked mechanism to describe subduction initiation, which goes back to *Howard* [1966] and *Fowler* [1985]. As stated by *Fowler* [1985]: " … consequently, the [thermal boundary] layer does not "see" the shear stress exerted by the interior flow (at leading order), and therefore the thermal boundary layer structure is totally self-determined … This fact makes it easy to analyze the problem, since the boundary layer uncouples from the rest of the flow." This idea, intrinsically used by many models [e.g., *Foley et al.*, 2012; *Turcotte*, 1995; *Wong and Solomatov*, 2015], assumes that the mantle below the thermal boundary layer (TBL) is passive and not actively driving subduction. If TBL thickening is the one and only mechanism for the onset of an overturn event in episodic convection, then that would predict that only normal stresses strongly increase immediately before the onset of overturn.

On the contrary, we find that the connection to the mantle below the TBL, leading to lateral flow and shear stress buildup, is crucial for plate yielding and subduction. The velocity profiles in Figure 4 show clearly that in the stagnant lid, basal shear increases continually in time leading up to failure and Figure 6 shows that although normal stress does increase, it does so only after the lithosphere has started to mobilize. This suggests that the initiation of an active lid mode is driven by basal shear stress increase.

3.2.2. Implications of a Basal Shear Stress World

Similarly to section 3.1.2, we now apply our 1-D model to study how the initiation of plate tectonics depends on planet mass and interior heat when basal shear stresses govern the transition from stagnant lid to active lid convection ($\tau_d = \tau_{zx}$). We find that for basal shear dominated systems, the behavior of plate yielding is similar for any reasonable value of model parameters (for values of β, γ, and ϵ see Appendix A). Therefore, for illustrative purposes, we focus on one set of parameter values for β and γ (to a first order, the basal shear stress model does not explicitly depend on ϵ, see Appendix A). For illustration, we use parameters based on no-slip boundary conditions at the lid base [$\beta = 1/5$, which with a lithospheric conductive cooling approach and $\epsilon = 0$ leads to $\gamma = 2/5$, *Stamenković and Breuer*, 2014].

For basal shear stress control, the initiation of plate tectonics is less likely with increasing planet mass when all planets start along the mantle solidus, as the red zone in Figure 7a remains always negative. This is also valid if all planets start along an adiabat. There is no unique trend in the scenario where massive planets can form anywhere between adiabatic and solidus temperatures (gray envelope in Figure 7), although there are more configurations where the initiation of plate tectonics is less likely on more massive planets. This distinct behavior for basal shear versus normal stress dominated model results from the different dependencies of shear and normal stresses on interior temperatures and viscosities, and hence on radiogenic heat concentration (compare Figure 2b with Figure 7b). For basal shear stress dominated systems, the initiation of plate tectonics becomes less likely when the concentration of interior heat sources increases (Figure 7b) (equivalent to *Stein et al.* [2013]). The principal reason for this behavior is that when interior temperatures increase, viscosity decreases, which leads to lower basal shear stress. The correlation that the initiation of plate tectonics is less likely for increasing heat sources is only valid if heat sources are not too scarce to prevent vigorous convection in the mantle—this seems generally a valid assumption for Earth mass and more massive planets for a variation of radiogenic heat sources of 0.1–10 times the Earth reference value when pressure effects on the viscosity are not too large [*Stamenković and Seager*, 2016].

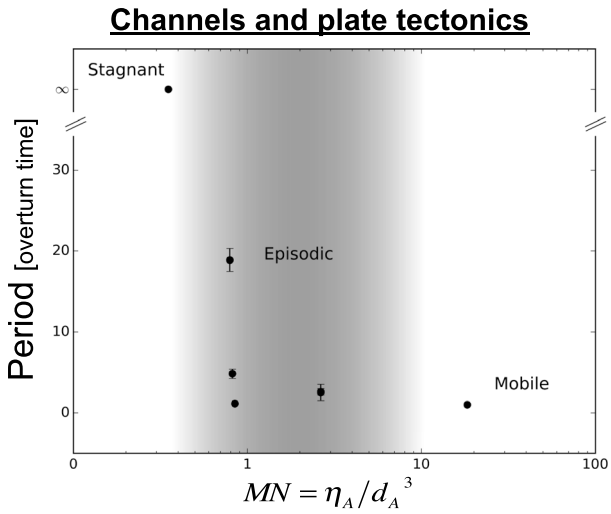

Figure 8. The importance of channel properties for the initiation of plate tectonics: All 3-D runs (summarized in Table 2, Runs 2 and 3 overlap on plot) are plotted as a function of channel number ($MN = \eta_A / d_A^3$) versus the overturn period (in mantle overturn time). There are no overturns in the stagnant lid regime, and hence, per definition its period between overturns is infinitely large; for plate tectonics overturns are continuous (therefore the period is 1 in overturn time), and episodic cases are between both extremes—suggesting a rule of thumb where decreasing MN values lead to smaller overturn rates—away from plate tectonics toward stagnant lid convection.

4. Discussion

A reason for differences in results between previous models studying the initiation of plate tectonics and our episodic mode approach comes from the fact that in our 3-D experiments the mantle is far from dynamic thermal equilibrium leading into plate failure. That is, the mantle is heating up significantly leading into failure due to an imbalance between heat generation and heat loss. The alternate modeling approach of studying failure from an initially statistical steady state stagnant lid configuration uses models that are in a dynamic thermal equilibrium with relatively small temperature and local stress variations about a mean value.

Which approach, the one close or the other far from thermal equilibrium, is a better representation for evolving planets? There is no single answer but we can make a case for the disequilibrium approach. For a planet coming out of magma ocean while still in a stagnant lid regime, it seems reasonable that the mantle goes through a heating up phase, as the planet is moving toward a dynamic equilibrium in terms of heat generation and loss [*Stamenković et al.*, 2012]. Along that path, the mantle could switch regimes before dynamic equilibrium is hit. The stagnant lid steady state approach cannot address that potential.

In the following, we discuss the implications of our results, elaborate on other sources of information that might help to better constrain the nature of stresses driving plate tectonics and critically evaluate our model's limitations, advantages, and robustness.

4.1. Channels Matter But Novel Causality Results Remain Robust

The assumption of a strong dehydrated lithosphere above a low-viscosity channel in the upper mantle allowed for channelization of lateral flow in the weak upper mantle [*Höink et al.*, 2011]. Without channels, convective stresses driving failure would be smaller (see Figures 5 and 8 and Table 2, which show that decreasing channel thicknesses lead the systems from stagnant lid over episodic to plate tectonics). This explains the generally larger stresses shown in Figure 6 compared to those typically found in other 3-D simulations and indicates that channels can help to overcome the discrepancy between experimentally derived lithospheric yield strengths and numerically derived convective stresses [see also *Richards et al.*, 2001]. As well as thickness, channel viscosity also impacts the convective flow and stress formation. Smaller channel viscosities enable better channelization but reduce the magnitude of convective stresses (compare Runs 2, 4, 6 shown in Figures 5 and 8).

We can use the runs we have at this stage to start mapping episodic, active, and stagnant behaviors as a function of channel parameters. As a metric, we consider the time between upper boundary layer overturn events relative to the average time it takes the interior mantle interior to overturn. This corresponds to the "period of overturn events" in units of overturn time (overturn time is defined in section 2.1). By definition, for an active lid mantle that will be one. Also by definition, it will be infinity for stagnant lid convection (the lid never overturns even if the rest of the mantle convects rapidly and overturns fast).

We empirically find that the period (in overturn time) increases with a decrease in a "channel number MN," which we define as $MN = \eta_A / (d_A)^3$ (here η_A is the nondimensional channel viscosity and d_A the ratio between channel thickness and mantle depth). This result is shown in Figure 8, where we plot for all runs specified in Table 2 the period of overturn events as a function of channel number MN. Decreasing values of MN

move the system toward larger periods and stagnant lid convection. So far, this observation is empirical. However, we note that in *Höink et al.* [2011], an asthenosphere Rayleigh number that is inversely proportional to our channel number has been defined. This connection might allow in the future to develop a more solid theory around this observation. At this stage, we can say that a decreasing channel number is associated with lower basal shear stress on the plate above, and in that sense, the results of Figure 8 are consistent with the idea that basal shear stress is critical for initiating plate failure.

One of our major results is that a strong time dependence of stresses and thermal disequilibrium leading into failure allow for a shift from normal to shear stresses leading the transition from a stagnant to an active lid mode. It is worth considering how sensitive this result is to the assumed channelization. As shown in *Höink et al.* [2012], channels allow a similar increase of both shear and normal stresses by a factor of ∼2 (up to maximally ∼10 if effects of the aspect ratio of convective cells are also considered). Therefore, although we do expect that it is more difficult to initiate failure and overturn events without channels, we do not expect that the ratio of shear to normal stresses is significantly affected by channels. Consequently, we also do not expect that our 1-D results would qualitatively change if we included channels in our 1-D model.

4.2. The Limits of Self-Determined Boundary Layer Dynamics

The breakdown of self-determined boundary layer stability ideas started to emerge with the numerical experiments of *Deschamps and Sotin* [2000] and the scaling analysis of *Moore* [2008], which indicated that boundary layer interactions could cause significant deviations from scaling ideas based on local stability analysis. Our results support those ideas, and we did observe hot rising instabilities, from the lower thermal boundary layer, interacting with the upper boundary layer. We also observed that lateral temperature variations, in the low-viscosity upper mantle, could generate pressure gradients that drove lateral flow [*Höink et al.*, 2011] and this, in turn, influenced upper boundary layer dynamics. Both of these effects are not consistent with the idea that the dynamics of the boundary layer are fully self determined. In terms of boundary layer interactions, our numerical experiments and those of *Deschamps and Sotin* [2000] were not run at extremely high Rayleigh numbers (the peak value from *Deschamps and Sotin* [2000] was $2 \cdot 10^7$).

The argument can be made that at higher Rayleigh numbers, boundary layer interactions could cease as hot thermals from the lower boundary layer might dissipate before they reach the upper boundary layer. However, numerical experiments to date [*Höink and Lenardic*, 2010] and theoretical analysis [*Höink et al.*, 2011] show no indication that the pressure flow declines with increasing convective vigor, as there is no physical reason for the pressure gradient work, which drives basal shear stress increase, to cease with increasing Rayleigh number even if plumes do not reach the base of the lithosphere. This suggests that our results are not limited to a particular region of Rayleigh number range.

The results from our 3-D experiments track the thermal boundary layer thickness, δ_{TBL}, and the internal temperature (so ΔT_{TBL} across the upper boundary layer) and can be used to determine a local upper thermal boundary layer Rayleigh number $Ra_{\mathrm{TBL}} = g\rho\alpha\Delta T_{\mathrm{TBL}}\delta_{\mathrm{TBL}}^3\kappa^{-1}\eta_{\mathrm{TBL}}^{-1}$, where η_{TBL} is the viscosity at the average temperature in the upper thermal boundary layer following *Richter* [1978]. Before failure, the upper thermal boundary layer thickness is 0.1 of the mantle depth and ΔT_{TBL} is about 0.9 of the total mantle temperature drop. As a conservative upper estimate for Ra_{TBL}, one can assume a temperature drop of 1 in the entire TBL; therefore, the upper TBL viscosity, η_{TBL}, will be (at least) a factor of 10 higher relative to the viscosity η_{ref} used to define $Ra_{3\text{-D}}$ from the depth-dependent part of the viscosity. Therefore, with the global 3-D model Rayleigh number being $Ra_{3\text{-D}} = 10^5$, we obtain an upper estimate for the upper TBL Rayleigh number $Ra_{\mathrm{TBL}} \sim Ra_{3\text{-D}}/(D/\delta_{\mathrm{TBL}})^3/(\eta_{\mathrm{TBL}}/\eta_{\mathrm{ref}}) < 10^5/10^3/10 = 10$. Note that this is before failure, as the local upper thermal boundary layer Rayleigh number Ra_{TBL} is changing throughout the experiment. The value of Ra_{TBL} just before overturn is about 2 orders of magnitude smaller than the critical Rayleigh number of ∼1000 predicted by local boundary layer stability analysis [*Howard*, 1966].

Following *Deschamps and Sotin* [2000] and *Stamenković et al.* [2012], such a smaller critical local Rayleigh number could be explained with the mantle below the upper TBL significantly impacting the formation of lithospheric instabilities. Based on the numerical scaling analysis of *Deschamps and Sotin* [2000], this would suggest that the Nusselt-Rayleigh scaling parameter β (see equations (A1) and (A2), a constant critical Rayleigh number, and free-slip boundary conditions), would be significantly smaller than its typical value of 1/3. The smaller Nusselt-Rayleigh parameter would represent a smaller cooling efficiency than commonly assumed for the same Rayleigh number. Also, the result that $\beta < 1/3$ brings into question results for

normal stress modes where $\beta = 1/3$ is explicitly assumed for the convective zone [e.g., *Foley et al.*, 2012; *Valencia et al.*, 2007]. A β value significantly smaller than 1/3 is in good agreement with various other studies with free-slip boundary conditions [e.g., *Bercovici et al.*, 1989; *Deschamps and Sotin*, 2000, and references therein; *Deschamps et al.*, 2010; *Moore*, 2008; *O'Neill et al.*, 2007; *Ratcliff et al.*, 1996; *Sotin and Labrosse*, 1999; *Stamenković and Breuer*, 2014; *Wolstencroft et al.*, 2009; *Yanagisawa and Yamagishi*, 2005].

4.3. Hints at Shear Stress Initiation But Open Questions Remain

Our 3-D results indicate a strong basal shear driven flow signature initiating overturn events and a strong coupling of the upper thermal boundary layer to the mantle below (Figures 4 and 6). Normal stresses at LAB start to significantly increase once the transition to active lid convection has occurred (see Figure 6). This is not in line with the idea that normal stresses fully control the transition from a stagnant to an active lid mode and lead to the hypothesis that the initiation of subduction could be driven by basal shear stresses and bottom-up yielding. In this bottom-up scenario, one could imagine that once yielding at the plate base has occurred, the subplate mantle system would start to cool and shear stress at the new plate base would further increase, allowing shear stresses to propagate upward to yield the plate bottom-up toward the surface.

We compute stresses at the LAB and hence do not resolve normal stresses in the upper lithosphere. Such stresses could potentially initiate top-down yielding. However, (1) the measured normal stress at the LAB is coupled to the normal stress within the plate and should therefore increase if the normal stress somewhere else in the plates increases, but we do not observe that and (2) the possibility of such top-down yielding depends critically on surface conditions. *Fowler* [1985] and *Solomatov* [2004] show that normal stresses are only large in a stress skin below the surface due to large lithospheric viscosity gradients induced by the strongly temperature-dependent viscosity. Following Solomatov [2004], for a thermal gradient with depth $\mathrm{d}T/\mathrm{d}z$ the stress skin depth δ_{stress} decreases significantly with viscosity contrast through the plate (with $\ln \Delta\eta = \theta$):

$$\delta_{\mathrm{stress}} \sim \theta^{-1}(\mathrm{d}T/\mathrm{d}z)^{-1} \tag{10}$$

The code we are using is limited to few orders of magnitude considering practical spatial resolutions and execution times. Realistic lithospheric viscosity contrasts before plate yielding could significantly exceed this value. Therefore, it is reasonable to suspect that the assumption of deeply reaching normal stresses are partially a peculiarity of small viscosity contrasts. This can be observed in *Foley and Bercovici* [2014] (compare their Figures 4 and 10), where normal stresses are pressed toward the surface with increasing viscosity contrast. Moreover, surface boundary conditions used in the majority of models to date can also overestimate the magnitude of normal stresses: so far, 2-D and 3-D models that find dominant normal stresses use a free-slip surface boundary condition, where shear stresses are per definition minimized and where normal stresses are allowed to freely evolve. The large normal stresses that result from free-slip models are most likely used to build dynamic topography, which balances the convective stress and thus maintains a stress-free surface [e.g., *Moresi and Parsons*, 1995]. This is in line with *Crameri and Tackley* [2015] who find that a free surface is more appropriate to model plate tectonics. It is therefore a crucial question whether for real planets normal stresses become even less important for the initiation of plate tectonics than what we found here. Our model does not allow for a free surface and cannot be used to test this issue at this stage.

There might be mechanisms where an increase in normal stress triggers an increase in shear stresses and causes overturn events, such as lithospheric thinning at an upflow, which could increase lid slope, possibly going into the direction of steady state stagnant lid based initiation models such as by *Wong and Solomatov* [2015]. Our results do not favor this, but to fully understand the feasibility of such a scenario, one needs appropriately designed time-dependent stress case experiments that focus on regions of lithosphere thinning and can resolve stress gradients in a lithosphere with a large viscosity contrast across it.

Furthermore, the data in Figure 6 indicate that although on average normal stresses dominate over basal shear stresses during the active lid phase, they do so only after the internal temperature reaches a maximum and starts to decrease (or Nusselt number increases). Just before the decrease in interior temperature, basal shear stress is generally larger than normal stress. If the turnover in interior temperature were to correspond to the onset of subduction, then this could indicate that the increase in normal stresses is a consequence but not a causal driver of subduction. However, clearly the data in Figure 6 lacks the resolution in time and in space needed to resolve this issue. Future studies will be designed to track spatial variations of stress components

and to incorporate tracking metrics that allow initial zones of failure to be isolated, so that local stresses can be monitored in those regions. This will allow us to study how, after a basal shear stress-driven transition from stagnant lid to plate tectonics like convection has occurred, shear and normal stresses causally correlate with plate failure and subduction.

5. Conclusions

We used 3-D experiments in an episodic mode to study the time-dependent nature of stresses across multiple overturn events and a 1-D thermal history model to study the implications for the initiation of plate tectonics as a function of stress type. In our 3-D model, the mantle is far from dynamic thermal equilibrium leading into plate failure versus alternate modeling approaches that start in dynamic equilibrium. That is a significnt difference, so it may be no surprise that results differ with our model favoring the conclusion that shear stress buildup initiates plate failure.

More specifically, we can draw three major conclusions from our results: (1) in dynamic disequilibrium and once stresses vary strongly in time increasing basal shear stresses drive the transition from stagnant to an active mode of convection; (2) the concept that upper thermal boundary layers are self determined, as commonly assumed and going back to *Howard* [1966] and *Fowler* [1985], is not supported; (3) the different stress controls (normal versus basal shear) for plate yielding lead to opposing conclusions for how plate tectonics depends on planet mass and interior heat.

Our study highlights the importance of strongly time variable stresses and dynamic disequilibrium for the initiation of plate failure and subduction and introduces a novel methodology to explore the origins of plate tectonics.

Appendix A: Additional 1-D Model Details

All parameterizations needed to reproduce our 1-D results can be found in equations (A1)–(A6), parameters are specified in Table 3. See Figure 1b–1d for illustrations. Please note that "$f[a]$" symbolizes that the function "f" depends on the variable "a." The 1-D model has been fully derived, defined, and discussed in *Stamenković et al.* [2012] (thermal evolution) and *Stamenković and Breuer* [2014] (plate tectonics aspects).

We study rocky planets of 1–10 Earth masses, with structures varying from a core to planet mass fraction of zero, over an Earth-like value, to 0.65 corresponding to Mercury. We use average material properties for mantle and core and mass-radius scalings (between planet radii and its mass) as described in *Stamenković et al.* [2012] for Earth-like planets and in *Stamenković and Seager* [2016] for non-Earth-like planets. The variation in thermal and transport properties in relation to Earth reference values is shown in Table 3 and is motivated by the results from *Stamenković and Seager* [2016] to characterize the diversity of rocky planets within our Galaxy. However, the range of planet conditions varied is not important for our conclusions, as the results remain the same for any studied planet model.

A1. One-Dimensional Thermal History Model

To compute the thermal evolution of a rocky planet, we couple an extended thermal boundary layer model for convective heat transport ((A1)–(A3)) to a conductive heat transport and stagnant lid growth equation (equation (A4)) and energy conservation in mantle and core [*Stamenković et al.*, 2012]. The model agrees well with 2-D numerical thermal evolution codes like GAIA [e.g., *Hüttig and Stemmer*, 2008].

$$\text{Rayleigh numbers} = \begin{cases} Ra = \alpha_m \rho_m g \tilde{D}^3 (T_l - T_m + T_c - T_b)(\kappa_m \tilde{\eta}_m)^{-1} \\ Ra_i = \alpha_m \rho_m g (R_p - R_c)^3 (T_s - T_m + T_c - T_b)(\kappa_m \tilde{\eta}_m)^{-1} \\ Ra^c_{\text{crit}} = 0.28 Ra_i^{0.21} \end{cases} \tag{A1}$$

$$\text{Heat flow} = \begin{cases} \delta_u = \tilde{D}(Ra/Ra_{\text{crit}})^{-\beta} \\ \delta_c = (\tilde{\eta}_c \kappa_m Ra^c_{\text{crit}} (\alpha_m \rho_m g \| T_c - T_b \|)^{-1})^{1/3} \\ q_m = k_m (T_m - T_l)/\delta_u \\ q_c = k_m (T_c - T_b)/\delta_c \\ q_s = -k_m (\partial T/\partial R)_{R=R_p} \end{cases} \tag{A2}$$

$$\text{Viscosity} = \left\{ \tilde{\eta}[T] = \tilde{\eta}_{\text{ref}} \exp\left(E^*/R_g\left(T^{-1} - T_{\text{ref}}^{-1}\right)\right)\right. \tag{A3}$$

$$\text{Stagnant lid} = \begin{cases} T_l[T_m] = T_m - 2.21 R_g T_m^2/E^* \\ \rho_m C_m (T_m - T_l) dL/dt = -q_m - k_m (\partial T/\partial R)_{R=R_l} \\ R^{-2}\partial(R^2 k_m \partial T/\partial R)/\partial R = -Q[t] \end{cases} \tag{A4}$$

The parameter g is the surface gravity, α_m is the average mantle thermal expansivity, ρ_m is the average mantle density, k_m is the average mantle thermal conductivity, C_m is the specific heat capacity at constant pressure, $\kappa_m = k_m/(\rho_m C_m)$ is the average mantle thermal diffusivity, R_g is the universal gas constant ~ 8.3145 J K^{-1} mol^{-1}, T_{ref} is the reference temperature, E^* the activation energy, and $\tilde{\eta}_{\text{ref}}$ is the reference viscosity of mantle rock, T_m is the upper mantle temperature, T_c is the core mantle boundary (CMB) temperature, $\tilde{\eta}(T)$ is the 1-D model temperature-dependent viscosity not to be confused with the viscosity used for the 3-D model (equation (1)), $\tilde{\eta}_m$ is the viscosity evaluated at the upper mantle temperature T_m, and $\tilde{D} = D - L$ is the depth of the convecting mantle. T is the temperature profile and R is the radial scalar, evaluated at the surface (R_p, T_s), at the core mantle boundary (R_c, T_c), or at the base of the stagnant lid (R_l, T_l).

We focus on the initiation of plate tectonics. Therefore, we have a stagnant lid of thickness $L[t]$ and base temperature $T_l = f[T_m]$ and study how easily plate failure can be initiated. There is approximately one order of magnitude of viscosity variation through the upper thermal sublayer that forms below the stagnant lid [*Davaille and Jaupart*, 1993; *Grasset and Parmentier*, 1998] (see equation (A4)).

The stagnant lid is above two unstable thermal boundary layers—one at the top δ_u, with base temperature T_m, and one at the bottom of the mantle δ_c with a temperature contrast of $\|T_c - T_b\|$. Please note that the 1-D definition of the upper thermal boundary layer does not include the stagnant lid and corresponds to the 3-D thermal sublayer. Both boundary layers drive convection via sinking cold and rising hot plumes, supported by secular cooling and internal heating $Q[t]$ due to radiogenic heat sources decaying in time. For the 1-D model values of $Q[t]$ in W/kg for Th, U, and K, see Table 4 in *Stamenković et al.* [2012], which are based on *McDonough and Sun* [1995]; note that in equation (A4) $Q[t]$ is in W m^{-3}. Between boundary layers, the temperature profile is assumed to be adiabatic due to vigorous convection. Our 1-D conclusions remain unchanged if we assume an isotherm instead, corresponding to our 3-D model's Boussinesq approximation.

The heat fluxes q_m from the convecting mantle into the stagnant lid and out of the core into the mantle q_c are computed via the boundary layer thicknesses and the linear temperature drops across those boundary layers (see equations (A1) and (A2)). The mantle heat flux is conducted through the stagnant lid, which is also heated by heat sources $Q[t]$. The surface heat flux q_s (equation (A2)) is determined via a steady state heat conduction equation (equation (A4)), as the typical relaxation time of the lithosphere, in the order of ~100 Myr, is much smaller than the relaxation time of the mantle of a few gigayears.

Note that our 1-D definition of *Ra*, the Rayleigh number for basally heated systems, uses $\tilde{\eta}_m[t]$ and the temperature drop over the two thermal boundary layers—not to be confused with the Rayleigh number in our 3-D model with a reference viscosity at the CMB.

The thermal boundary layers scale as functions of the Rayleigh number, *Ra*, and the internal Rayleigh number Ra_i (equation (A1)), a constant critical Rayleigh number, Ra_{crit}, of 1000, and the Nusselt-Rayleigh exponent β, which depends on boundary conditions, mode of heating, *Ra* number regime, and the degree of upper and lower mantle interaction (see *Stamenković and Breuer* [2014], for a summary). In the core (red zone in Figure 1b), we assume adiabatic temperatures. To compute the core heat flux and the lower thermal boundary layer thickness (equation (A2)), it has been shown that for a strongly temperature-dependent viscosity it is more appropriate to evaluate the viscosity $\tilde{\eta}_c$ at the average temperature within the lower thermal boundary layer and to use a local instability criterion [i.e., *Deschamps and Sotin*, 2000; *Richter*, 1978]. The thermal evolution of rocky planets and the propensity of plate tectonics using temperature-dependent viscosity is not significantly affected by the specific choice of the lower mantle parameterization, as the lower mantle quickly self-adjusts [*Stamenković et al.*, 2012; *Stamenković and Breuer*, 2014]. This changes for a strongly pressure-dependent lower mantle viscosity [*Stamenković and Breuer*, 2014], which we do not consider here.

A2. One-Dimensional Plate Yielding Model

To study the efficiency of initiating plate yielding as a function of planet mass and radiogenic heat content, we (1) start with the failure function X (equation (8)) and compute it as a function of driving stress being either dominated by $\tau_d = \tau_{zz}$ for normal stresses or $\tau_d = \tau_{zx}$ for basal shear stresses with the scalings from equations (A5) and (A6). In a second step, we compute the propensity of plate tectonics for a change in planet condition from A → B as the ratio of the failure functions at conditions B and A (see equation (8)).

$$\text{Velocity and geometry} = \begin{cases} v_c \sim \kappa_{up}\tilde{D}^{-1}(Ra/Ra_{\text{crit}})^{\gamma} \\ \Lambda \sim \tilde{D}(Ra/Ra_{\text{crit}})^{-\epsilon} \end{cases} \tag{A5}$$

$$\text{Driving and yield stresses} = \begin{cases} \tau_{zx} = \tilde{\eta}_m \partial v_c/\partial R \sim \tilde{\eta}_m \tilde{D}^{-1} v_c \\ \tau_{zz} = \tau_{xx} = \tau_{zx}\Lambda(L+\delta_u)^{-1} \\ \tau_y = g\rho_{\text{up}} C_{\text{fric}}(L+\delta_u) \end{cases} \tag{A6}$$

v_c is the convective velocity at the base of the thermal lithosphere of thickness $L+\delta_u$ scaling with a parameter γ, Λ is the length of convective cells (approximately plate length scaling with ϵ), τ_{zx} is the shear stress acting on the base of the thermal lithosphere, τ_{zz} is the normal stress in the thermal lithosphere classically computed from a force balance equation between shear and normal stresses in steady state, τ_y is the Byerlee yield stress at the base of the thermal lithosphere [*Byerlee*, 1968], C_{fric} is the lithospheric friction coefficient, and ρ_{up} is the lithosphere density, assumed not to scale with planet mass [based on *Sotin et al.*, 2007] and $\kappa_{\text{up}} = k_m/(\rho_{\text{up}} C_m)$. Replacing ρ_{up} with ρ_m for all scalings does not affect our results, which are dominated by viscosity and thermal conductivity variations.

A3. Model Parameters: $(\beta, \gamma, \epsilon)$

Our 1-D scalings depends mainly on whether $\tau_d = \tau_{zz}$ or $\tau_d = \tau_{zx}$ but also on the thermal evolution parameters $(\beta, \gamma, \epsilon)$: reasonable values for $(\beta, \gamma, \epsilon)$ are $1/5 < \beta < 1/3$, $1/3 < \gamma < 2/3$, and $0 < \epsilon < 1/6$ and are in agreement with all 3-D an 2-D numerical simulations assuming reasonable mantle rock rheologies and theoretical constraints from evolution models for the Earth [e.g., *Deschamps and Sotin*, 2000, and references therein; *Deschamps et al.*, 2010; *Lenardic et al.*, 2006; *Moore*, 2008; *O'Neill et al.*, 2007; *Parmentier and Sotin*, 2000; *Ratcliff et al.*, 1996; *Sotin and Labrosse*, 1999; *Stamenković and Breuer*, 2014; *Wolstencroft et al.*, 2009; *Yanagisawa and Yamagishi*, 2005; *Zhong*, 2005]. Values of β much smaller than 1/5 or even negative [*Korenaga*, 2003] have not been confirmed by 2-D or 3-D numerical experiments to date, and as such, we did not explore them. Most frequently values of $\beta = 1/3$, $\gamma = 2/3$, and $\epsilon = 0$ are used.

Acknowledgments

This work was supported by a fellowship from the Simons Foundation (award 338555, VS) and by the NSF grant EAR-0944156 (A.L. and T.H.). Simulation data are available upon request. We thank two anonymous reviewers for their suggestions and their support.

References

Bercovici, D., G. Schubert, G. A. Glatzmaier, and A. Zebib (1989), Three-dimensional thermal convection in a spherical shell, *J. Fluid Mech.*, *206*, 75–104.

Buffett, B. A., H. E. Huppert, J. R. Lister, and A. W. Woods (1996), On the thermal evolution of the Earth's core, *J. Geophys. Res.*, *101*, 7989–8006.

Byerlee, J. D. (1968), Brittle-ductile transition in rocks, *J. Geophys. Res.*, *73*, 4741–4750.

Christensen, U. (1984), Convection with pressure- and temperature-dependent non-Newtonian rheology, *Geophys. J. R. Astron. Soc.*, *77*, 343–384.

Crameri, F., and P. J. Tackley (2015), Parameters controlling dynamically self-consistent plate tectonics and single-sided subduction in global models of mantle convection, *J. Geophys. Res. Solid Earth*, *120*, 3680–3706, doi:10.1002/2014JB011664.

Davaille, A., and C. Jaupart (1993), Transient high-Rayleigh-number thermal convection with large viscosity variations, *J. Fluid Mech.*, *253*, 141–166.

Deschamps, F., and C. Sotin (2000), Inversion of two-dimensional numerical convection experiments for a fluid with a strongly temperature-dependent viscosity, *Geophys. J. Int.*, *143*, 204–218.

Deschamps, F., P. J. Tackley, and T. Nakagawa (2010), Temperature and heat flux scalings for isoviscous thermal convection in spherical geometry, *Geophys. J. Int.*, *182*, 137–154.

Escartin, J., G. Hirth, and B. Evans (2001), Strength of slightly serpentinized peridotites: Implications for the tectonics of oceanic lithosphere, *Geology*, *29*, 1023–1026.

Foley, B. J., and T. W. Becker (2009), Generation of plate-like behavior and mantle heterogeneity from a spherical, viscoplastic convection model, *Geochem. Geophys. Geosyst.*, *10*, Q08001, doi:10.1029/2009GC002378.

Foley, B. J., and D. Bercovici (2014), Scaling laws for convection with temperature-dependent viscosity and grain-damage, *Geophys. J. Int.*, *199*, 580–603.

Foley, B. J., D. Bercovici, and W. Landuyt (2012), The conditions for plate tectonics on super-Earths: Inferences from convection models with damage, *Earth Planet. Sci. Lett.*, *331-332*, 281–290.

Fowler, A. C. (1985), Fast thermoviscous convection, *Stud. Appl. Math.*, *72*, 189–219.

Grasset, O., and E. M. Parmentier (1998), Thermal convection in a volumetrically heated, infinite Prandtl number fluid with strongly temperature-dependent viscosity: Implications for planetary thermal evolution, *J. Geophys. Res.*, *103*, 18,171–18,181.

Grott, M., and D. Breuer (2008), The evolution of the Martian elastic lithosphere and implications for crustal and mantle rheology, *Icarus*, *193*, 503–515.
Hirth, G., and D. L. Kohlstedt (1996), Water in the oceanic upper mantle: Implications for rheology, melt extraction and the evolution of the lithosphere, *144*, 93–108.
Höink, T., and A. Lenardic (2010), Long wavelength convection, poiseuille-couette flow in the low-viscosity asthenosphere and the strength of plate margins, *Geophys. J. Int.*, *180*, 23–33.
Höink, T., A. M. Jellinek, and A. Lenardic (2011), Asthenosphere drive: A wavelength-dependent plate-driving force from viscous coupling at the lithosphere-asthenosphere boundary, *Geochem. Geophys. Geosyst.*, *12*, Q0AK02, doi:10.1029/2011GC003698.
Höink, T., A. Lenardic, and M. A. Richards (2012), Depth-dependent viscosity and mantle stress amplification: Implications for the role of the asthenosphere in maintaining plate tectonics, *Geophys. J. Int.*, *191*, 30–41, doi:10.1111/j.1365-24X2012.o5621.x.
Howard, L. N. (1966), Convection at high Rayleigh numbers, in *Proceedings of the Eleventh International Congress of Applied Mathematics*, edited by H. Gortler, pp. 1109–1115, Springer, New York.
Hüttig, C., and K. Stemmer (2008), Finite volume discretization for dynamic viscosities on Voronoi grids, *Phys. Earth. Planet. Inter.*, *171*, 137–146.
Korenaga, J. (2003), Energetics of mantle convection and the fate of fossil heat, *Geophys. Res. Lett.*, *30*, 1437–1440.
Korenaga, J. (2010), On the likelihood of plate tectonics on super-Earths. Does size matter?, *Astrophys. J. Lett.*, *725*, 43–46.
Lenardic, A., and W. M. Kaula (1994), Tectonic plates, D″ thermal structure, and the nature of mantle plumes, *J. Geophys. Res. B*, *99*, 15,697–15,708.
Lenardic, A., M. A. Richards, and F. H. Busse (2006), Depth-dependent rheology and the horizontal length scale of mantle convection, *J. Geophys. Res.*, *111*, B07404, doi:10.1029/2005JB003639.
Loddoch, A., C. Stein, and U. Hansen (2006), Temporal variations in the convective style of planetary mantles, *Earth Planet. Sci. Lett.*, *251*, 79–89.
McDonough, W. F., and S.-S. Sun (1995), The composition of the Earth, *Chem. Geol.*, *120*, 223–253.
McWilliams, R. S., et al. (2012), Phase transformations and metallization of magnesium oxide at high pressure and temperature, *Science*, *338*, 1330–1333.
Moore, W. B. (2008), Heat transport in a convecting layer heated from within and below, *J. Geophys. Res.*, *113*, B11407, doi:10.1029/2006JB004778.
Moresi, L., and B. Parsons (1995), Interpreting gravity, geoid, and topography for convection with temperature dependent viscosity: Application to surface features on Venus, *J. Geophys. Res.*, *100*, 21,155–21,171.
Moresi, L., and V. S. Solomatov (1998), Mantle convection with a brittle lithosphere: Thoughts on the global tectonic styles of the Earth and Venus, *Geophys. J. Int.*, *133*, 669–682.
von Mises, R. (1913), Mechanik der festen Körper im plastisch deformablen Zustand, *Göttin. Nachr. Math. Phys.*, *1*, 582–592.
O'Neill, L. A., and A. Lenardic (2007), Geological consequences of super-sized Earths, *Geophys. Res. Lett.*, *34*, L19204, doi:10.1029/2007GL030598.
O'Neill, C., M. Jellinek, and A. Lenardic (2007), Conditions for the onset of plate tectonics on terrestrial planets and moons, *Earth Planet. Sci. Lett.*, *261*, 20–32.
O'Rourke, J. G., and J. Korenaga (2012), Terrestrial planet evolution in the stagnant-lid regime: Size effects and the formation of self-destabilizing crust, *Icarus*, *221*, 1043–1060.
Parmentier, E. M., and C. Sotin (2000), Three-dimensional numerical experiments on thermal convection in a very viscous fluid: Implications for the dynamics of a thermal boundary layer at high Rayleigh number, *Phys. Fluids*, *12*, 609–617.
Ratcliff, J. T., G. Schubert, and A. Zebib (1996), Steady tetrahedral and cubic patterns of spherical shell convection with temperature-dependent viscosity, *J. Geophys. Res.*, *101*, 25,473–25,484.
Richards, M., W.-S. Yang, J. R. Baumgardner, and H.-P. Bunge (2001), Role of a low-viscosity zone in stabilizing plate tectonics: Implications for comparative terrestrial planetology, *Geochem. Geophys. Geosyst.*, *2*, 1026.
Richter, F. M. (1978), Mantle convection models, *Annu. Rev. Earth Planet. Sci.*, *6*, 9–19.
Solomatov, V. S. (2004), Initiation of small-scale convection, *J. Geophys. Res.*, *109*, B01412, doi:10.1029/2003JB002628.
Sotin, C., and S. Labrosse (1999), Three-dimensional thermal convection in an iso-viscous, infinite Prandtl number fluid heated from within and from below: Applications to the transfer of heat through planetary mantles, *Phys. Earth Planet. Inter.*, *112*, 171–190.
Sotin, C., O. Grasset, and A. Mocquet (2007), Mass-radius curve for extrasolar Earth-like planets and ocean planets, *Icarus*, *191*, 337–351.
Stamenković, V., D. Breuer, and T. Spohn (2011), Thermal and transport properties of mantle rock at high pressure: Applications to super-Earths, *Icarus*, *216*, 572–596.
Stamenković, V., L. Noack, D. Breuer, and T. Spohn (2012), The infuence of pressure-dependent viscosity on the thermal evolution of Super-Earths, *Astrophys. J.*, *748*, 41–62.
Stamenković, V., and D. Breuer (2014), The tectonic mode of rocky planets: Part 1—Driving forces, models, and parameters, *Icarus*, *234*, 174–193.
Stamenković, V., and S. Seager (2016), Emerging possibilities and insuperable limitations of exogeophysics: The example of plate tectonics, *Astrophys. J.*, in press.
Stein, C., J. Schmalzl, and U. Hansen (2004), The effect of rheological parameters on plate behaviour in a self-consistent model of mantle convection, *Phys. Earth Planet. Inter.*, *142*, 225–255.
Stein, C., J. P. Lowman, and U. Hansen (2013), The influence of mantle internal heating on lithospheric mobility: Implications for super-Earths, *Earth Planet. Sci. Lett.*, *361*, 448–459.
Stevenson, D. J., T. Spohn, and G. Schubert (1983), Magnetism and thermal evolution of the terrestrial planets, *Icarus*, *54*, 466–489.
Tackley, P. (2000), Self-consistent generation of tectonic plates in time-dependent, three-dimensional mantle convection simulations: 1. Pseudoplastic yielding, *Geochem. Geophys. Geosyst.*, *1*, 1026.
Tan, E., E. Choi, P. Thoutireddy, M. Gurnis, and M. Aivazis (2006), Geoframework: Coupling multiple models of mantle convection within a computational framework, *Geochem. Geophys. Geosyst.*, *7*, Q06001, doi:10.1029/2005GC001155.
Trompert, R., and U. Hansen (1998), Mantle convection simulations with rheologies that generate plate-like behavior, *Nature*, *395*, 686–688.
Turcotte, D. L. (1995), How does Venus lose heat?, *J. Geophys. Res.*, *100*, 16,931–16,940.
Turcotte, D. L., and G. Schubert (2002), *Geodynamics*, 2nd ed., 458 pp., Cambridge Univ. Press, New York.
Valencia, D., R. J. O'Connell, and D. D. Sasselov (2007), Inevitability of plate tectonics on super-Earths, *Astrophys. J. Lett.*, *670*, 45–48.
Wolstencroft, M., J. H. Davies, and D. R. Davies (2009), Nusselt-Rayleigh number scaling for spherical shell Earth mantle simulation up to a Rayleigh number of 10^9, *Phys. Earth Planet. Inter.*, *176*, 132–141.

Wong, T., and V. S. Solomatov (2015), Towards scaling laws for subduction initiation on terrestrial planets: Constraints from two-dimensional steady-state convection simulations, *Prog. Earth Planet. Sci.*, *2*, 18–51.

Yanagisawa, T., and Y. Yamagishi (2005), Rayleigh-Bénard convection in spherical shell with infinite Prandtl number at high Rayleigh number, *J. Earth Simul.*, *4*, 11–17.

Zhong, S., M. T. Zuber, L. Moresi, and M. Gurnis (2000), Role of temperature-dependent viscosity and surface plates in spherical shell models of mantle convection, *J. Geophys. Res.*, *105*, 11,063–11,082.

Zhong, S. (2005), Dynamics of thermal plumes in three-dimensional isoviscous thermal convection, *Geophys. J. Int.*, *162*, 289–300.

Erratum

In the originally published version of this article, there was one error in Table 1 and one error in Table 2. In Table 1, in the "Units" column, "W kg^{-3}" has been changed to "W kg^{-1}." In Table 2, text that was included as a separate footnote has now been included as part of the Table caption. These errors have since been corrected and this version may be considered the authoritative version of record.